# Continuum Simulations of Acetylcholine Diffusion with Reaction-determined Boundaries in Neuromuscular Junction Models

Yuhui Cheng [a,*], Jason K. Suen [a], Zoran Radić [b], Stephen D. Bond [d], Michael J. Holst [c], J. Andrew McCammon [a,b]

[a]*Department of Chemistry and Biochemistry, Center for Theoretical Biological Physics, National Biomedical Computation Resource, and Howard Hughes Medical Institute,*

[b]*Department of Pharmacology,*

[c]*Department of Mathematics, University of California, San Diego, La Jolla, CA 92093-0365, USA*

[d]*Department of Computer Science, University of Illinois at Urbana-Champaign, Urbana, IL 61801, USA*

## Abstract

The reaction-diffusion system of the neuromuscular junction has been modeled in 3D using the finite element package FEtk. The numerical solution of the dynamics of acetylcholine with the detailed reaction processes of acetylcholinesterases and nicotinic acetylcholine receptors has been discussed with the reaction-determined boundary conditions. The simulation results describe the detailed acetylcholine hydrolysis process, and reveal the time-dependent interconversion of the closed and open states of the acetylcholine receptors as well as the percentages of unliganded/monoliganded/diliganded states during the neurotransmission. The finite element method has demonstrated its flexibility and robustness in modeling large biological systems.

*Key words:* finite element method, synaptic transmission, substrate inhibition, reaction-determined boundaries
*1991 MSC:* 74S05, 65M50, 65M60

* Corresponding author. Address: Department of Chemistry and Biochemistry, University of California, San Diego, 9500 Gilman Dr. MC 0365, La Jolla, CA 92093-0365, U.S.A., Tel.: (858)822-2771, Fax: (858)534-4974

  *Email addresses:* ycheng@mccammon.ucsd.edu (Yuhui Cheng), suenj@alum.mit.edu (Jason K. Suen), zradic@ucsd.edu (Zoran Radić), sdbond@uiuc.edu (Stephen D. Bond), mholst@cam.ucsd.edu (Michael J. Holst), jmccammon@ucsd.edu (J. Andrew McCammon).

# 1 Introduction

The nature of neuronal signaling has been a problem of special interest in both biology and neuroscience (1–4). During neurotransmission, a neurotransmitter must be released from the terminal bouton of the presynaptic neuron, diffuse cross the synaptic gap, and activate postsynaptic receptors.

The neuromuscular junction (NMJ), the point of communication between neurons and muscle fiber, provides a classic example of synaptic transmission. The terminals of motor axons contain thousands of vesicles filled with acetylcholine (ACh). When an action potential reaches the axon terminal, hundreds of these vesicles discharge their ACh molecules onto a specialized area of postsynaptic membrane on the fiber. This area contains a cluster of transmembrane channels, i.e. the nicotinic acetylcholine receptors (nAChRs), which are opened by the association of ACh; sodium or potassium ions ($Na^+$ & $K^+$) can then diffuse through the channels, $Na^+$ inward and $K^+$ outward (5–9).

ACh molecules remain in the cleft between the presynaptic and postsynaptic membranes until they are hydrolyzed by acetylcholinesterase (AChE), the biomolecular off-switch for synaptic transmission. AChE is present as clusters of three tetramers suspended by collagen stalks bound to the muscle membrane at varying densities (600 $\mu m^{-2}$ to 2500 $\mu m^{-2}$) throughout the junctional folds (JFs). Acetylcholinesterase breaks down the ACh in the neuromuscular junction at a maximum speed of ∼2000 ACh molecules per second per AChE active site in the case of human enzyme. Therefore, it provides a very efficient mechanism to terminate synaptic transmission for subsequent signaling (10, 11). Drug molecules such as competitive inhibitors can bind with AChE and regulate the breakdown rate of ACh and affect the subsequent signaling rate and strength.

The receptor nAChR is a ligand-gated sodium channel that opens briefly upon binding ACh. This allows entry of sodium ions into the interior of the muscle cell, which results in partial depolarization of the postsynaptic membrane. If the number of open channels reaches the proper threshold, a self-propagating muscle action potential is generated in the postsynaptic membrane. nAChRs are present in small quantities over most of the muscle membrane surface but are concentrated heavily at the tips of the NMJs.

In adult NMJ, nAChR is a transmembrane pentamer consisting of 5 subunits assembled with a stoichiometry $\alpha_2\beta\gamma\delta$ around an axis of pseudosymmetry perpendicular to the plane of the membrane (9, 12). One nAChR pentamer has two activation binding sites for ACh: one lies at the interface between one $\alpha$ and the $\gamma$ subunit while the other is between the second $\alpha$ subunit and the $\delta$ subunit (9, 12). The binding of ACh molecules to the binding sites induces the ion channel to open. Spontaneous opening of a single vesicle causes generation of the miniature end-

plate current (mEPC).

Simulations of partial differential equation (PDE) based synapse models have provided a great deal of insight into several aspects of synaptic transmission (13–20). However, these models assumed the synapse to be two dimensional only and employed relatively out-of-date kinetic models for ACh hydrolysis and state changes of nAChR. These limitations are largely due to the complexity of solving three dimensional (3D) PDEs with complex boundary conditions (21–25). Recently, solutions of 3D PDEs in synaptic transmission models became possible with the advance of finite element methods (26–29). However, simple AChE reaction models have been used, and the nAChRs were not treated explicitly. On the other hand, stochastic or Monte Carlo (MC) based models such as that embedded in the MCell software enables 3D NMJ simulations with realistic kinetic models for ACh hydrolysis and binding and dissociation (30–32). In this paper, we report a complementary approach to the MC model to describe the behavior of a NMJ based on a 3D PDE with recent kinetic models for ACh hydrolysis and the various nAChR conformational changes initiated by ACh binding. Competitive inhibitors of AChE can also be integrated with the AChE reaction model. Our approach allows coupling of the detailed chemical reactions with the physical diffusion processes taking place during synaptic transmission. We can model many more physiological phenomena in the ACh diffusion, such as substrate and competitive inhibition, and the conformational variations of nAChR. In addition, simulation of surface dynamics at the postsynaptic membrane could be incorporated. Therefore, our approach shall enable pharmacokinetics and pharmacodynamics analysis of rationally designed drugs involving synaptic transmission. Implementation of the numerical algorithm for simulating the NMJ model was performed using FEtk and the Manifold Code (33).

## 2   Model setup and mathematical background

### 2.1   The AChE model

The kinetic model for ACh hydrolysis is built based on a mechanism proposed by Radić et al. (34–36) (Fig. 1 (d)). This model incorporates the effect of substrate inhibition and therefore enables an accurate representation of the reaction over a large range of ACh concentrations. In Fig. 1 (d), E and S represent AChE and ACh respectively. S combines at two discrete sites, forming two binary complexes, ES (ACh in the active site) and SE (ACh in the peripheral site (34, 37)), only one of which, ES, results in substrate hydrolysis. The following values of the kinetic parameters were used in this study: $k_s^+ = k_{ss}^+ = 10^9 M^{-1} s^{-1}$, $k_s^- = 4.6 \times 10^4 s^{-1}$, $k_{ss}^- = 1.5 \times 10^7 s^{-1}$, $k_{cat} = 1.4 \times 10^5 min^{-1}$, and b = 0.23.

Assuming AChEs are fixed in space, the conservation equations for describing the various states of AChE with a given ACh concentration on the surface are:

$$\frac{d\theta_1}{dt} = k_s^+ p(x,t)(1 - \sum_{i=1}^{3} \theta_i) + k_{ss}^- \theta_3 - (k_s^- + k_{ss}^+ p(x,t) + k_{cat})\theta_1$$

$$\frac{d\theta_2}{dt} = k_{ss}^+ p(x,t)(1 - \sum_{i=1}^{3} \theta_i) + k_s^- \theta_3 - (k_s^+ p(x,t) + k_{ss}^-)\theta_2$$

$$\frac{d\theta_3}{dt} = k_s^+ p(x,t)\theta_2 + k_{ss}^+ p(x,t)\theta_1 - (k_s^- + k_{ss}^- + bk_{cat})\theta_3 \tag{1}$$

Here, $\theta_1$, $\theta_2$, $\theta_3$ and $1 - \sum_{i=1}^{3} \theta_i$ denote the normalized concentrations of ES, SE, SES and E, respectively, relative to the total concentration of AChE involved intermediates and products, $[AChE]_{total}$; p(x,t) represents ACh concentration in the position "x" at time "t". Solution procedure for the above ordinary differential equations (ODEs) is outlined in the "Supplementary Material".

In addition to the reaction mechanism, an important attribute in modeling NMJ is the representation of the AChE structure in space. As in our previous effort of using rectilinear AChE model(27, 28), we represent an AChE cluster including 3 AChE tetramers using a cubic box with 1/8 of the surface considered to be active. In terms of the PDE model for ACh diffusion, the active boundary is implemented by a Robin boundary (radiation or essential boundary) with $\theta_1$, $\theta_2$ and $\theta_3$ calculated from Eq. 1, while other parts of the AChE cluster are represented by the Neumann boundary (reflecting boundary) (Fig. 1 (c)).

The binding level of ACh to AChE that gives rise to a specific intermediate is monitored by the integral of the total fraction of that given intermediate on the reactive surfaces of AChE, $L_i$(t),

$$L_i(t) = \int_{\partial\Omega_{AChE}^{act}} \theta_i(t)dS \tag{2}$$

Here $\partial\Omega_{AChE}^{act}$ is the surface of the active site of AChE. With i = 1, 2, 3, we are able to observe general timescale trends of all AChE intermediates.

The nAChR is a heteropentameric trans-membrane protein that protrudes into the synaptic and intracellular compartments, with a five-fold axis of quasi-symmetry perpendicular to the membrane. Measured from the separations of the Cys-loop disulfide bonds, the average protomer-protomer separation (the distance between two nearby subunit centers) is around 29 Å (38). The side length of the extracellular domains including the ligand-binding region and the interface is around 70 Å (7).

Experimental studies on nAChR have shown several conformations under physiological conditions. At least three different conformations have been differentiated: the closed state (C), the open state (O) and the desensitized state (D). These conformations can interconvert with one another. Among the different nAChR conformations, the desensitized state is still elusive experimentally. Therefore to illustrate the feasibility of our approach, this work focuses on using a simple nAChR gating process, based on the experimental reaction scheme suggested by Land et al. (39). With ACh occupying the binding sites, the closed $\rightleftharpoons$ open reaction ("gating") of the diliganded nAChR is much more favorable ($\Theta = \beta/\alpha \cong 28$) than that of unliganded receptor ($\Theta \cong 10^{-7} - 10^{-6}$) (40). Here, $\alpha$ and $\beta$ are the rate constants for opening and closing, respectively. The affinity of the nAChR for ACh is circa 12,000-fold higher in the open than in the closed conformation. Based on the kinetic measurements, the reaction mechanism corresponding to different conformation states of nAChR are shown in Fig. 2 (b).

The conservation equations of all the different conformations of nAChR in Fig. 2 (b), with a given concentration of ACh on the active surface of nAChR are,

$$
\begin{aligned}
\frac{\mathrm{d}\phi_1}{\mathrm{d}t} &= 2k_+ p(x,t)\left(1 - \sum_{i=1}^{3}\phi_i\right) + 2k_- \phi_2 - (k_- + k_+ p(x,t))\phi_1 \\
\frac{\mathrm{d}\phi_2}{\mathrm{d}t} &= k_+ p(x,t)\phi_1 + \beta\phi_3 - (2k_- + \alpha)\phi_2 \\
\frac{\mathrm{d}\phi_3}{\mathrm{d}t} &= \alpha\phi_2 - \beta\phi_3
\end{aligned}
\tag{3}
$$

Where $\phi_1$, $\phi_2$ and $\phi_3$ represent the fractions of the monoliganded receptors $[AR^{1or2}]$, and the diliganded receptors [C] and [O] relative to the total concentration of nAChR, i.e. we define $[R_{total}] = [AR^{1or2}] + [C] + [O] + [R^0]$, $\phi_1 = [AR^{1or2}]/[R_{total}]$, $\phi_2 = [C]/[R_{total}]$ and $\phi_3 = [O]/[R_{total}]$, Therefore, $[R^0] = 1 - \sum_{i=1}^{3}\phi_i$.

The corresponding kinetic parameters (39, 41, 42) for our simulation are:

$$k_+ = k_{+1} = k_{+2} = k_{+3} = k_{+4} = 3.0 \times 10^7 M^{-1} s^{-1};$$
$$k_- = k_{-1} = k_{-2} = k_{-3} = k_{-4} = 1.0 \times 10^4 s^{-1};$$
$$\alpha = 2.0 \times 10^4 s^{-1};$$
$$\beta = 5.0 \times 10^3 s^{-1}; \tag{4}$$

The detailed solution to the above equations is similar to that for the AChE kinetic equations.

To represent the complex morphology of nAChR pentamers, we modeled each nAChR pentamer as pentagonal prism and placed the pentamer at the bottom of a large cubic box (Fig. 2). Specifically, the length of the edge of the top or bottom pentagons is 5.84 $n$m and the length of the side of the pentagonal prism is 7.0 $n$m. All the pentagonal prisms were placed at the base of a cubic box with 0.50 $\mu$m edges (Fig.3). For each nAChR pentagonal prism, mixed boundary conditions were employed. The active-site boundaries $\partial\Omega^{act}_{nAChR}$ were distributed on two sides of the pentagonal prism, of which only 1/8 of each side is defined as the active site, i.e. the ACh-binding site. When coupled with the ACh diffusion dynamics, the boundary condition at the active sites of nAChR were assumed to be Robin boundary conditions with $\phi_i$ evaluated using Eq. 3, whereas the remaining surface of nAChR was modeled as Neumann boundary conditions.

To model large quantities of nAChRs, the pentameric nAChR is currently too expensive for computation. Therefore, we consider a tetrahedral nAChR instead of a pentameric nAChR. Two faces of each tetrahedron are labeled as ACh binding sites. The total surface area of the tetrahedron is determined by matching the correlation of the ion-channel maximum open probabilities with ACh concentration using the pentameric nAChR (Fig. 7). The surface area of the tetrahedron is found to be around $1.2 \times 10^{-4} \mu m^2$.

### 2.3 *Weak formulation of the time-dependent diffusion equations*

In this section, we present the weak formulations of the time-dependent diffusion equations for use in the finite element calculations (43, 44).

Let $\Omega$ be the computational domain of the NMJ model and denote $\partial\Omega$ as the boundary. The strong form of the diffusion equation of our NMJ model (27, 28) for the ACh dynamics is:

$$\frac{\partial p(x,t)}{\partial t} = \nabla \cdot D \nabla p(x,t) \text{ in } \Omega \tag{5}$$

With boundary conditions read as,

$$\hat{n} \cdot D \nabla p(x,t) = \begin{cases} -k'_{act,AChE}[k_s^+(1 - \sum_{i=1}^3 \theta_i)p(x,t) - \frac{k_s^- \theta_1}{p(x,0)}], & \text{on } \partial\Omega_{AChE}^{act} \\ -k'_{act,nAChR}(k_{bind}^+ p(x,t) - k_{bind}^-), & \text{on } \partial\Omega_{nAChR}^{act} \\ 0, & \text{otherwise} \end{cases} \tag{6}$$

Where $k'_{act,AChE}$ and $k'_{act,nAChR}$ are defined as the AChE and nAChR reaction coefficients respectively, which were determined by sampling (see Section 3.1 below); $k_{bind}^+ = k_+[2(1 - \sum_{i=1}^3 \phi_i) + \phi_1]$, and $k_{bind}^- = \frac{k_-(\phi_1 + 2\phi_2)}{p(x,0)}$. $\partial\Omega_{nAChR}^{act}$ corresponds to a single ACh binding site boundary on a nAChR and $p(x,0)$ is the initial concentration of ACh. The intermediates for ACh hydrolysis $\{\theta_i\}$ and the different nAChR conformation states $\{\phi_i\}$ are determined through the corresponding sets of ODEs (Eq. 1 and 3) with ACh concentration evaluated at the corresponding boundaries. Following the definition in Holst et al. (45) and Cheng et al. (46), the "weak" formulation reads as

Find $p(x,t) \in V$ such that

$$< F(p(x,t)), v >= 0 \ \forall v \in V, \tag{7}$$

where

$$< F(p(x,t)), v >= \int_\Omega (D\nabla p(x,t) \cdot \nabla v + \frac{\partial p(x,t)}{\partial t} v)dx$$
$$- \int_{\partial\Omega_{AChE}^{act}} (-k'_{act,AChE}[k_s^+(1 - \sum_{i=1}^3 \theta_i)p(x,t) - \frac{k_s^- \theta_1}{p(x,0)}])dS$$
$$- \int_{\partial\Omega_{nAChR}^{act}} (-k'_{act,nAChR}(k_{bind}^+ p(x,t) - k_{bind}^-))dS$$
$$\tag{8}$$

### 2.4 The neuromuscular junction model

A complete NMJ model includes a vesicle fused to the presynaptic membrane, a primary cleft, AChE clusters and nAChR pentamers. AChE clusters consisting of three AChE tetramers are represented explicitly in the mesh as a cubic box with $1/8$ of the surface being active. The nAChR pentamers are modeled as pentagonal prisms placed at the bottom of a large cubic box with active sites occupying $1/8$ of the surface on two sides of each pentagonal prism, representing the independent

treatment of the two ACh binding sites. To elucidate the geometric influence of the NMJ on the system dynamics, two different NMJ models have been prepared in this study.

The first NMJ model (denoted as Model I) presented in Fig. 4 consists of 8 explicit cubic AChE clusters and 750 nAChR pentamers. The vesicle fused to the middle of the presynaptic membrane is modeled as a sphere of radius 0.024 $\mu m$ centered at 0.016 $\mu m$ above this membrane, leaving a circular area of radius 0.018 $\mu m$ as the pore opening. The dimensions of the primary cleft are 0.30 $\mu m$ (length), 0.10 $\mu m$ (width) and 0.10 $\mu m$ (height). The depth of the junction fold (JF) is 1.0 $\mu m$. 750 nAChR pentameric prisms are evenly distributed on the inner surface of the primary cleft and JF. The density of nAChR on the postsynaptic membrane of the primary cleft is circa 10,000 $\mu m^{-2}$. In the JF, from the crest to 0.25 $\mu m$ into the fold, the density remains at 10,000 $\mu m^{-2}$, and then falls off to 5,000 $\mu m^{-2}$ over another 0.4 $\mu m$, below which the density decreases dramatically until zero. 8 AChE clusters were put in the space of the primary cleft and JF, which represented 96 AChE monomers.

The second model (denoted as Model II) is depicted in Fig 5. 323 cubic AChE and 29462 tetrahedral nAChRs are integrated. The tetrahedral nAChR models are developed similarly to the pentameric ones (see section 3.2), but reduce the computational demands. Model II includes a vesicle with the same size as Model I but with a different amount of AChE and nAChR. The length, width and height of the primary cleft for Model II are 0.95 $\mu m$, 2.0 $\mu m$ and 0.1 $\mu m$, respectively. The depth of the junction fold (JF) is 0.8 $\mu m$. 29462 tetrahedral nAChRs (see Section 3.2 below) are placed on the surface of the primary cleft and JF. The density setup is the same as in the above model. 323 AChE clusters are integrated in the space of the primary cleft and JF, representing 3876 AChE monomers.

*2.5   Numerical solution scheme for the complete NMJ model*

Spatial approximation of the NMJ cleft space is performed by using a finite element method. The physical domain $\Omega$ of the NMJ cleft space is divided into a collection of tetrahedra by using NETGEN (47), a flexible mesh generation package. The detailed discretized weak formulation is listed in "Supplementary Material".

The numerical solution of the above NMJ models is achieved by an iterative method to solve the 3D diffusion problem with reaction-determined boundaries. At each time step, the ACh concentration is first updated with the intermediates corresponding to different states of AChE and nAChR. Specifically, numerical solution of the linear algebraic problem arose from the temporal discretization with $\{\theta_i\}$ and $\{\phi_i\}$ evaluated at the previous time step is solved by using the conjugate gradient method with tolerance of $10^{-10}$. Then with the updated ACh concentration profile, the var-

ious states of AChE and nAChR are evaluated by the solution of the corresponding kinetic equations of ACh binding. The spatial independence of the different states of AChE and nAChR enables a nodal solution for the ACh kinetic equations, for which we employed analytical solution to invert the linear algebraic problem raised from the temporal discretization using the Crank-Nicholson scheme. To ensure convergence and adequate resolution of the reaction kinetics and postsynaptic response, timesteps ranging from $10^{-1}$ $\mu s$ to $10^1$ $\mu s$ were used for the simulation. We have also attempted other solution schemes for solving the coupled ODE/PDE system and found that the current numerical scheme provided the best balance between overall stability and the computational demand of the solution algorithm. It takes less than 10 minutes to complete 1,000 timesteps on a single Intel Xeon 3.60GHz CPU for a system of ~20,000 vertices (Model I).

*2.6 Evaluation of the various states and conformations of the nAChR ion channel*

nAChR can exist in unliganded, monoliganded and diliganded states. We evaluate the flux of ACh binding to the two active sites as,

$$I(t) = \int_{\partial\Omega_{nAChR}^{act}} k'_{act,nAChR}(k_{bind}^+ p(x,t) - k_{bind}^-)dS \qquad (9)$$

The integration area is over the two ACh binding sites for each nAChR.

The number of bound ACh molecules (or postsynaptic coverage) can then be defined as the accumulating quantity of ACh:

$$N(t) = \int_0^t I(\tau)d\tau \qquad (10)$$

A receptor with $N(t) \geq 2$ represents the diliganded state, while $1 \leq N(t) < 2$ the monoliganded state and $0 \leq N(t) < 1$ the unliganded state.

The partial number of open channels in one ACh binding site of a nAChR can be calculated using the average value of $\phi_3$.

$$p(O)^I = \frac{\int_{\partial\Omega^I_{nAChR}} \phi_3 dS}{\int_{\partial\Omega^I_{nAChR}} dS}$$

$$p(O)^{II} = \frac{\int_{\partial\Omega^{II}_{nAChR}} \phi_3 dS}{\int_{\partial\Omega^{II}_{nAChR}} dS} \tag{11}$$

Here "I" and "II" denote the two ACh binding sites of one nAChR pentamer (Fig. 2 (a)).

Then the partial number of open channels for one nAChR is $p(O) = p(O)^I + p(O)^{II}$, and the nominal (equivalent) number of open channels in the NMJ cleft is $N(O) = N_{nAChR}p(O)$.

## 3   Results and Discussion

### 3.1   Reactivity of the AChE

In this section, we compare the reactivity of the AChE model with experimental results by considering an *in silico* experiment by computing the reaction rate constant of an isolated AChE cluster confined in a cubic box. The concentration of ACh at the boundary of the cubic box is assumed to be constant. Specifically, we place an AChE cluster as described in Section 2 at the center of a cube with 0.30 *μm* edges. The boundary condition for $\partial\Omega^{act}_{AChE}$ in Eq. 7 is used on the surface of the interior cube, the AChE cluster. On the exterior cube boundary $\partial\Omega$ - $\partial\Omega^{act}_{AChE}$, the concentration of ACh is held at a different constant value for each "trial" simulation. At steady state, the analytical reaction rate of an AChE monomer can be written in the reaction scheme depicted in Fig. 1 (d):

$$\upsilon(t \to \infty) = [AChE]_0 \left(\frac{k_{cat}}{1+\frac{K_m}{p(x,t)}}\right)\left(\frac{1+\frac{bp(x,t)}{K_{ss}}}{1+\frac{p(x,t)}{K_{ss}}}\right) \tag{12}$$

Here $k_{cat} = (1.4 \pm 0.1) \times 10^5 min^{-1}$, $K_m = \frac{k_s^-}{k_s^+} = 46 \pm 3\mu M$ and $K_{ss} = \frac{k_{ss}^-}{k_{ss}^+} = 15 \pm 2mM$.

The recent calculations on an isolated AChE tetramer (48) suggest the reaction activity of one AChE cluster is approximately equivalent to that of 9 independent AChE monomers. Therefore, the analytical reaction rate of one AChE cluster $V(t \to \infty) = 9\upsilon(t \to \infty)$.

Following the mechanism in Fig. 1 (d), the reaction rate at each node of one AChE active site is

$$\upsilon_i(t) = [AChE]_0 k_{cat}(\theta_1 + b\theta_3) \tag{13}$$

Therefore, the average reaction rate of one AChE cluster is

$$\upsilon(t) = \frac{\int \sum_{i=1}^{N_{tot}} \upsilon_i(t) dS}{\int 1 dS} \tag{14}$$

From the above equations, $k'_{act,AChE}$ can be determined by evaluating $V(\infty) = \lim_{t \to \infty} \upsilon(t)$ for ACh concentration on the outer boundary ranging from 0.01 $mM$ to 100 $mM$. Fig. 6 suggests an excellent agreement between the experimental and computational reaction rates (34). Based on these results, we deduce $k'_{act,AChE} = 1.50 \times 10^{-5} M \cdot m^{-2}$.

### 3.2  Reactivity of the nAChR

Now we consider another *in silico* experiment by considering the behavior of nAChR. Specifically, 625 nAChRs are evenly placed at the base center of a large cubic box with 0.5 $\mu m$ edges (Fig. 3). Except the side with the embedded nAChRs (Neumann or reflecting boundary), all other sides are assigned as Dirichlet constant concentration boundaries. ACh molecules fill the space inside the cubic box with the initial concentration at 10.0 $\mu$M, 30.0 $\mu$M, 60.0 $\mu$M, 100.0 $\mu$M for each trial, respectively.

Evaluation of the ion-channel maximum open probabilities under different initial ACh concentrations using Eq. 11 yields the results shown in Fig.7. All the open percentages have been calibrated with the experimental data in (49). Following Smart and McCammon et al.(1998), $k'_{act,nAChR}$ can finally be determined as $6.6 \times 10^{-6} M \cdot m^{-2}$.

### 3.3  The complete NMJ models

We simulated Model I (Fig. 4) with an initial ACh distributed only inside the vesicle to examine the dynamics of the ACh, AChE and conformational chances of nAChR. The initial concentration of ACh of 300 $mM$ corresponds to a ACh density of $1.8 \times 10^8 \mu m^{-3}$ (27, 28, 50–52). The time evolution of ACh is monitored to elucidate insights for the neurotransmission process.

Fig. 8 depicts the time course of the total number of ACh molecules during the

first 20 *ms* following the release of ACh into the junction. With the complete kinetic model in this work, the overall time course can be separated into two phases. The first phase corresponds to approximately the first 1.5 *ms* following release. During this phase, the number of ACh molecules in the model drops dramatically due to rapid binding of ACh to both AChE and nAChR. In the second phase ($t \geq 1.5ms$), ACh concentration decays gradually due to the "slower" consumption of ACh through hydrolysis by AChE. If only a linear reaction rate is used for ACh hydrolysis and ACh-nAChR binding is assumed to be at equilibrium (dotted line in Fig. 8), then only a gradual consumption of ACh is observed. This is consistent with the previous observation by Tai et al. (28).

Comparing with previous studies (27, 28), the reactive boundaries in the present work are determined by the kinetics of ACh binding to AChE or nAChR. The AChE kinetics in response to a quantal release of ACh are shown in Fig. 9. The amounts of three AChE complexes have been determined with timesteps of 0.1 $\mu$s. The high accumulation of the complex ES (ACh in the active site) suggests that most of ACh are trapped as this intermediate and the complete hydrolysis of ACh may take much longer. On the other hand, the amount of SE (ACh in the peripheral site) stays near zero after the first few $\mu$s. The relative amount of SES (ACh in both the active and peripheral sites) remains less than 10% of ES. This suggests that the substrate inhibition in the NMJ might be negligible in the case of single vesicle release.

Previous work didn't explicitly model nAChRs on the postsynaptic membrane. Here, not only two nAChR models have been proposed, but also various nAChR conformations have been analyzed. In Model I, the nAChR pentamers undergo continuous conformational changes during the simulation (Fig. 10). Fig. 10 (c) indicates that the number of the unliganded nAChRs exponentially decreases to below 200 during the first 20 $\mu$s of simulation. The number of monoliganded nAChR jumps to nearly 200 in a short time and rapidly decays to below 25. Most of the nAChRs rapidly become diliganded. It takes around 150$\mu$s to 200 $\mu$s for the whole system to reach a nearly steady state with about 700 nAChRs in the diliganded conformation. The number of closed state diliganded receptors increases to above 200 in the first 15 $\mu$s, and then decays exponentially. The open state shows a parabola-shaped increase to a maximum, and then the number of open channels slowly decreases. It must be noted that most of the nAChR receptors keep two ACh bound during 1 *ms* of simulation. The dissociation rate of ACh from the diliganded state is quite slow in experiments (>1 s).

We also tested model sensitivities by varying the number of AChE clusters in the model. Fig.11 shows the effect of modulating the density of AChE. The number of open channels gradually reduces along with the increase of AChE clusters, which aligns well with physical intuition and is qualitatively consistent with observations by using Monte Carlo simulation (32).

To validate the above observation from the simulation results, we extended our

study on Model II (Fig. 5). Fig. 12 shows the time courses of all the AChE intermediates and the number of open channels. The qualitatively consistent trends suggest similar dynamics and behavior to Model I, but geometric features of the primary cleft and the distribution of AChE clusters and nAChRs play an important role in determining the quantitative feature of the pharmacokinetics and pharmacodynamics analysis. It takes around 100 $\mu s$ to reach the nearly steady state. Around 300 of 323 AChE clusters remain in the ES complex state. Meanwhile, the maximal open percentage of nAChR decreases to 0.3% while above 95% in Model I. This is reasonable since we have a large number of AChE clusters and nAChRs in Model II.

## 4  Conclusions

In this work, 3D neuromuscular junction models with explicit geometric details of both AChEs and nAChRs have been studied with the finite element method. By considering detailed kinetic processes of AChE and nAChR, time-dependent conformational state conversion of the nAChR can be observed during the simulations. In addition, through comparison with simple kinetic models in previous works, we discovered unique characteristics in the consumption of ACh in a neuromuscular junction after the release of a quanta of ACh into the synapse.

Our simulation results suggest that model geometry and size have profound effects on the postsynaptic nAChR open probabilities, implying that the quantal release can have different amplification characteristics with the fixed amount of ACh. Comparing with the 2D NMJ model in Naka et al.(17, 53), our 3D models revealed additional detailed information and features during ACh diffusion, binding and hydrolysis. We derived a numerical solution strategy for solving the system of partial differential equations (describing ACh diffusion) with time dependent, ODE based boundary conditions (describing ACh hydrolysis and ACh-nAChR binding/dissociation). Such reaction-diffusion coupling models might aid future pharmacokinetics studies for NMJ-related diseases by considering the activities of compounds at both AChE and AChR. To this end, both 3D geometry and comprehensive kinetic models are essential for an integrative NMJ model.

During the 15 $ms$ simulation, the dynamics of ACh in the synaptic cleft might be characterized into two stages. In the first stage, ACh molecules bind with nAChRs while some of them are destroyed by AChE. Then AChE removes the unreacted ACh from the synaptic cleft in a subsequent stage. Our results further support previous observations that most of the neurotransmitters will be eliminated before subsequent rebinding to nAChR can occur (39, 54, 55). In addition, although the concentration of ACh in the vesicle is much higher than 1 mM, the overall ACh concentration at the AChE clusters after one quantal ACh release never reaches 1 mM, therefore, the ACh substrate inhibition might be negligible in the case of

13

single vesicle release.

The ACh binding with nAChRs occurs within 5 $\mu s$ after a ACh quantal release. nAChRs undergo several conformation changes and then some channels will open to conduct $Na^+/K^+$ ions. In our simulations, the number of unliganded, monoliganded and diliganded ion channels has been recorded along with the simulation time. Additionally, the time course of open channels is traced and analyzed for the diliganded ion channels.

While our simulation results reveal many of the features in ACh diffusion in a neuromuscular junction upon the release of a quanta of ACh from the presynaptic membrane, a major shortcoming in the current work is that the model does not take into account stochasticity and discrete processes occurring in the NMJ. The local concentration of ACh is of order $\mu M$ and therefore the number of ACh molecules surviving for few of $\mu s$ after release of one vesicle may range from 100 to 1000. This number of ACh molecules makes the continuum assumption approximate. However, our preliminary results for comparing stochastic and deterministic models suggests qualitative similarities between these two methods for the same synapse model. Given the computationally efficient nature of deterministic models and finite element methods, our model is a reasonable alternative to stochastic methods for studying cholinergic synaptic transmission.

To illustrate the principle and usefulness of our approach, we focused our effort on models with relatively simple pre/post-synaptic membrane geometries. Despite the lack of realism of the NMJ model, our simulation is capable of capturing the geometrical difference, and extending the software for simulating large and realistic meshes replicating complex NMJ structures as observed by electronmicroscopy is straightforward. Constructing large and realistic meshes requires powerful adaptive meshing methods that are capable of reconstructing real NMJ structures. Part of this work has recently proven to be possible as with the adaptive meshing tool of "Mol-LIBIE" by Zhang et al. (56). The development of such models will enable a realistic description of synapse activity, as well as modeling the interplay between morphological changes of the synapse, chemical and molecular reactions of AChE and nAChR, and ACh diffusion in the complicated geometry.

Of equal importance to building a realistic synapse model is to construct detailed kinetic models for both AChE hydrolysis and AChE-nAChR binding. These kinetic models represents both the kinetic events happened during the reaction, as well as the molecular conformation changes of the enzyme and receptors. A detailed understanding of these events will enable modeling of different AChE and nAChR mutations, as well as catalyze the development of pharmaceutical agents for various NMJ diseases. Of specific interest is to describe desensitized conformations for complementing new experimental findings through kinetic modeling of nAChR. Moreover, the role of substrate inhibition of AChE in synaptic activity can be examined through releasing large numbers of quanta. Some of these topics are

currently under investigation and will be described in forthcoming manuscripts.

## 5 Acknowledgments

## References

[1] J. C. Wathey, M. M. Nass, H. A. Lester, Numerical reconstruction of the quantal event at nicotinic synapses, Biophys. J. 27 (1) (1979) 145–164.

[2] A. Friboulet, D. Thomas, Reaction diffusion coupling in a structured system - application to the quantitative simulation of end-plate currents, J. Theor. Biol. 160 (4) (1993) 441–455.

[3] T. Nagado, K. Arimura, Y. Sonoda, A. Kurono, Y. Horikiri, A. Kameyama, M. Kameyama, O. Pongs, M. Osame, Potassium current suppression in patients with peripheral nerve hyperexcitability, Brain 122 (1999) 2057–2066.

[4] A. B. Smit, N. I. Syed, D. Schaap, J. van Minnen, J. Klumperman, K. S. Kits, H. Lodder, R. C. van der Schors, R. van Elk, B. Sorgedrager, K. Brejc, T. K. Sixma, W. P. M. Geraerts, A glia-derived acetylcholine-binding protein that modulates synaptic transmission, Nature 411 (6835) (2001) 261–268.

[5] M. Harel, R. Kasher, A. Nicolas, J. M. Guss, M. Balass, M. Fridkin, A. B. Smit, K. Brejc, T. K. Sixma, E. Katchalski-katzir, J. L. Sussman, S. Fuchs, The binding site of acetylcholine receptor as visualized in the X-ray structure of a complex between alpha-bungarotoxin and a mimotope peptide, Neuron 32 (2) (2001) 265–275.

[6] S. M. Sine, A. G. Engel, Recent advances in cys-loop receptor structure and function, Nature 440 (7083) (2006) 448–455.

[7] A. Miyazawa, Y. Fujiyoshi, N. Unwin, Structure and gating mechanism of the acetylcholine receptor pore, Nature 423 (6943) (2003) 949–955.

[8] N. Unwin, Structure and action of the nicotinic acetylcholine receptor explored by electron microscopy, FEBS Lett. 555 (1) (2003) 91–95.

[9] N. Unwin, Refined structure of the nicotinic acetylcholine receptor at 4 angstrom resolution, J. Mol. Biol. 346 (4) (2005) 967–989.

[10] P. Taylor, Anticholinesterase agents, in: The Pharmacological Basis of Therapeutics, McGraw-Hill, New York., 1996, pp. 161–176, j. G. Hardman, L. E. Limbird, P. B. Molinoff, R. W. Ruddon, and A. G. Gilman, editors.

[11] T. Shen, K. Tai, R. Henchman, J. A. McCammon, Molecular dynamics of acetylcholinesterase, Acc. Chem. Res. 35 (6) (2002) 332–340.

[12] A. Karlin, Emerging structure of the nicotinic acetylcholine receptors, Nat. Rev. Neurosci. 3 (2) (2002) 102–114.

[13] R. Bertram, A simple model of transmitter release and facilitation, Neural. Comput. 9 (3) (1997) 515–523.

[14] R. Bertram, A. Sherman, E. F. Stanley, Single-domain/bound calcium hypothesis of transmitter release and facilitation, J. Neurophysiol. 75 (5) (1996) 1919–1931.

[15] P. J. Kruk, H. Korn, D. S. Faber, The effects of geometrical parameters on synaptic transmission: a monte carlo simulation study, Biophys. J. 73 (6) (1997) 2874–2890.

[16] L. M. Wahl, C. Pouzat, K. J. Stratford, Monte Carlo simulation of fast excitatory synaptic transmission at a hippocampal synapse, J. Neurophysiol. 75 (2) (1996) 597–608.

[17] T. Naka, N. Sakamoto, Localization effects of acetylcholine release from a synaptic vesicle at the neuromuscular junction, Biosystems 51 (2) (1999) 73–78.

[18] T. Ghaffari-farazi, J. S. Liaw, T. W. Berger, Consequence of morphological alterations on synaptic function, Neurocomputing 26-7 (1999) 17–27.

[19] T. Naka, Evaluation of characteristic parameters for the neurotransmitter release mechanisms at the neuromuscular junction, Biosystems 49 (2) (1999) 143–149.

[20] T. Naka, Simulation analysis of the effects of the junctional folds on spontaneous generation of the miniature endplate current at neuromuscular junction, Math. Comput. Simul. 46 (5-6) (1998) 631–639.

[21] S. Aharon, M. Bercovier, H. Parnas, Parallel computation enables precise description of Ca2+ distribution in nerve terminals, Bull. Math. Biol. 58 (6) (1996) 1075–1097.

[22] R. L. Cooper, J. L. Winslow, C. K. Govind, H. L. Atwood, Synaptic structural complexity as a factor enhancing probability of calcium-mediated transmitter release, J. Neurophysiol. 75 (6) (1996) 2451–2466.

[23] W. M. Yamada, R. S. Zucker, Time course of transmitter release calculated from simulations of a calcium diffusion-model, Biophys. J. 61 (3) (1992) 671–682.

[24] H. Parnas, G. Hovav, I. Parnas, Effect of $Ca^{2+}$ diffusion on the time course of neurotransmitter release, Biophys. J. 55 (5) (1989) 859–874.

[25] R. S. Zucker, N. Stockbridge, Pre-synaptic calcium diffusion and the time courses of transmitter release and synaptic facilitation at the squid giant synapse, J. Neurosci. 3 (6) (1983) 1263–1269.

[26] O. Axelsson, V. A. Baker, Finite element solution of boundary value problems, in: Theory and Computation, Academic Press, San Diego, 1984.

[27] J. L. Smart, J. A. McCammon, Analysis of synaptic transmission in the neuromuscular junction using a continuum finite element model, Biophys. J. 75 (4) (1998) 1679–1688.

[28] K. Tai, S. D. Bond, H. R. Macmillan, N. A. Baker, M. J. Holst, J. A. McCammon, Finite element simulations of acetylcholine diffusion in neuromuscular junctions, Biophys. J. 84 (4) (2003) 2234–2241.

[29] D. Braess, in: Finite Elements, Cambridge University Press, Cambridge,

1997.

[30] J. R. Stiles, T. M. Bartol, Monte Carlo methods for simulating realistic synaptic microphysiology using MCell, in: E. D. Schutter (Ed.), Computational Neuroscience: Realistic Modeling for Experimentalists, CRC Press, Inc., New York, 2000, pp. 87–127.

[31] J. R. Stiles, T. M. Bartol, M. M. Salpeter, T. J. Sejnowski, Synaptic variability: new insights from reconstructions and Monte Carlo simulations with MCell, in: W. M. Cowan, T. C. Sudhof, C. F. Stevens (Eds.), Synapses, Johns Hopkins University Press, Baltimore, Maryland., 2001, pp. 681–731.

[32] J. S. Coggan, T. M. Bartol, E. Esquenazi, J. R. Stiles, S. Lamont, M. E. Martone, D. K. Berg, M. H. Ellisman, T. J. Sejnowski, Evidence for ectopic neurotransmission at a neuronal synapse, Science 309 (5733) (2005) 446–451.

[33] M. Holst, Adaptive numerical treatment of elliptic systems on manifolds, Adv. Comput. Math. 15 (1-4) (2001) 139–191.

[34] Z. Radić, N. A. Pickering, D. C. Vellom, S. Camp, P. Taylor, 3 distinct domains in the cholinesterase molecule confer selectivity for acetylcholinesterase and butyrylcholinesterase inhibitors, Biochemistry 32 (45) (1993) 12074–12084.

[35] Z. Kovarik, Z. Radić, H. A. Berman, V. Simeon-rudolf, E. Reiner, P. Taylor, Acetylcholinesterase active centre and gorge conformations analysed by combinatorial mutations and enantiomeric phosphonates, Biochem. J. 373 (2003) 33–40.

[36] Z. Radić, P. Taylor, Interaction kinetics of reversible inhibitors and substrates with acetylcholinesterase and its fasciculin 2 complex, J. Biol. Chem. 276 (7) (2001) 4622–4633.

[37] Y. Bourne, P. Taylor, Z. Radic, P. Marchot, Structural insights into ligand interactions at the acetylcholinesterase peripheral anionic site, Embo J. 22 (1) (2003) 1–12.

[38] N. Unwin, A. Miyazawa, J. Li, Y. Fujiyoshi, Activation of the nicotinic acetylcholine receptor involves a switch in conformation of the a subunits, J. Mol. Biol. 319 (5) (2002) 1165–1176.

[39] B. R. Land, W. V. Harris, E. E. Salpeter, M. M. Salpeter, Diffusion and binding constants for acetylcholine derived from the falling phase of miniature endplate currents, Proc. Natl. Acad. Sci. U. S. A. 81 (5) (1984) 1594–1598.

[40] C. Grosman, A. Auerbach, The dissociation of acetylcholine from open nicotinic receptor channels, Proc. Natl. Acad. Sci. U. S. A. 98 (24) (2001) 14102–14107.

[41] F. N. Salamone, M. Zhou, A. Auerbach, A re-examination of adult mouse nicotinic acetylcholine receptor channel activation kinetics, J. Physiol.-London 516 (2) (1999) 315–330.

[42] C. Grosman, F. N. Salamone, S. M. Sine, A. Auerbach, The extracellular linker of muscle acetylcholine receptor channels is a gating control element, J. Gen. Physiol. 116 (3) (2000) 327–339.

[43] S. Fucik, A. Kufner, in: Nonlinear differential equations, Elsevier Scientific Publishing Company, New York., 1980.

[44] W. Hackbusch, in: Elliptic differential equations, Springer-Verlag, Berlin, Germany, 1994.

[45] M. Holst, N. Baker, F. Wang, Adaptive multilevel finite element solution of the poisson-boltzmann equation i. algorithms and examples, J. Comput. Chem. 21 (15) (2000) 1319–1342.

[46] Y. H. Cheng, J. Suen, D. Q. Zhang, S. Bond, Y. J. Zhang, Y. H. Song, N. Baker, C. Bajaj, M. Holst, J. A. McCammon, Finite element analysis of the time-dependent smoluchowski equation for acetylcholinesterase reaction rate calculations, Biophys. J. accepted.

[47] J. Schöberl, Netgen: an advancing front 2D/3D-mesh generator based on abstract rules, Comput. Visual Sci. 1 (1997) 41–52.

[48] D. Q. Zhang, J. Suen, Y. J. Zhang, Y. H. Song, Z. Radić, P. Taylor, M. J. Holst, C. Bajaj, N. A. Baker, J. A. Mccammon, Tetrameric mouse acetyl-cholinesterase: continuum diffusion rate calculations by solving the steady-state Smoluchowski equation using finite element methods, Biophys. J. 88 (3) (2005) 1659–1665.

[49] G. Akk, A. Auerbach, Activation of muscle nicotinic acetylcholine receptor channels by nicotinic and muscarinic agonists, Br. J. Pharmacol. 128 (7) (1999) 1467–1476.

[50] J. H. Schwartz, Synaptic vesicles, in: E. R. Kandel, J. H. Schwartz, T. M. Jessell (Eds.), Principles of Neural Science, Appleton and Lange, Norwalk, Connecticut., 1991, pp. 225–234.

[51] H. Zimmermann, in: Synaptic Transmission: Cellular and Molecular Basis, Thieme, Stuttgart, Germany, 1993.

[52] T. C. Südhof, R. H. Scheller, Mechanism and regulation of neurotransmitter release., in: Synapses, Johns Hopkins University Press, Baltimore, Maryland., 2000, w. M. Cowan, T. C. Südhof, and C. F. Stevens, editors.

[53] T. Naka, K. Shiba, N. Sakamoto, A two-dimensional compartment model for the reaction-diffusion system of acetylcholine in the synaptic cleft at the neuromuscular junction, Biosystems 41 (1) (1997) 17–27.

[54] K. L. Magleby, D. A. Terrar, Factors affecting time course of decay of end-plate currents - possible cooperative action of acetylcholine on receptors at frog neuromuscular-junction, J. Physiol.-London 244 (2) (1975) 467–495.

[55] B. Katz, R. Miledi, Binding of acetylcholine to receptors and its removal from synaptic cleft, J. Physiol.-London 231 (3) (1973) 549–574.

[56] Y. J. Zhang, C. Bajaj, B. S. Sohn, 3d finite element meshing from imaging data, Comput. Meth. Appl. Mech. Eng. 194 (48-49) (2005) 5083–5106.

**Figure Legends**

Figure 1. (a) A cluster of three AChE tetrameters suspended by collagen stalks bound to the muscle membrane; (b) An AChE tetramer with four active sites exposed; (c) The AChE cluster representing Fig. 1(a), the blue surface denotes the nonreactive Neumann boundary, while yellow corresponds to the reactive Robin boundary; (d) The AChE kinetic scheme. S represents ACh, while ES and SE represent the binary complexes with ACh in the active site and peripheral site, respectively.

Figure 2. (a) View of the finite element mesh of the nAChR and part of the external box. Two red triangles represent two ACh binding sites and are assigned the reactive boundary, and all other green triangles belong to non-active sites and are assigned the neumann boundary; (b) The nAChR kinetic scheme. $R^0$ denotes the unliganded nAChR, $AR^1$ or $AR^2$ denotes the monoliganded nAChR; C and O represent diliganded closed and open states.

Figure 3. Two views of the finite element mesh for the nAChR model. (a) the outside of the model, with the 625 nAChRs integrated at the bottom of the rectangular box. (b) a close up view of the bottom surface with the nAChR pentamers.

Figure 4. Three views of the finite element mesh for Model I, with one secondary cleft and a spherical vesicle fused to the presynaptic membrane. The cubic boxes represent AChE, and pentameric prisms represent nAChR. (a) outside view; (b) inside of the primary cleft; (c) inside of the secondary cleft. The length unit is $\mu m$.

Figure 5. Two views of the finite element mesh for Model II, in which each nAChR is represented as a tetrahedron. (a) outside view; (b) inside of the primary and secondary clefts. The length unit is $\mu m$.

Figure 6. Concentration dependencies of the AChE activity in both the experiment and this work.

Figure 7. The maximal open probabilities of the ion channel under different ACh concentrations for the pentameric, tetrahedral nAChR and the experiment, respectively.

Figure 8. Total number of ACh molecules in Model I, comparing with the simple AChE kinetic model in the previous work (28).

Figure 9. The time course of three AChE complexes in Model I: ES, SE and SES represent complexes that the substrate ACh occupies the active site, the peripheral site and both two sites, respectively.

Figure 10. The Number of various nAChR conformations in Model I: $R^0$ denotes the unliganded nAChR, $AR^{1or2}$ the monoliganded nAChR, C and O the diliganded closed and open nAChR, respectively.

Figure 11. Effect of varying the number of AChE clusters on the number of open channels in Model I.

Figure 12. Finite element solutions of Model II: (a) and (b) Number of all the AChE complexes; (c) Number of open channels.
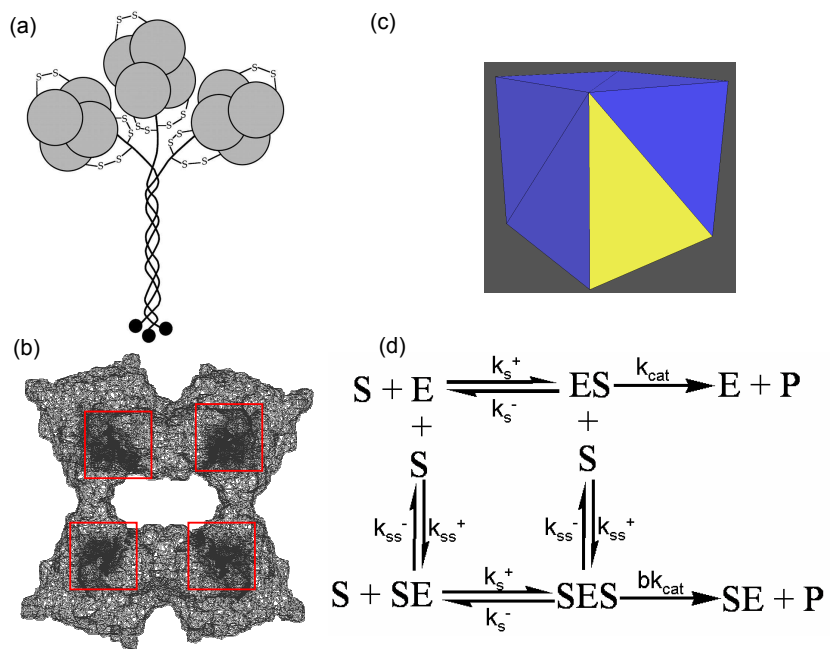
Fig. 1.

(a)

(c)

(b)

(d)

$$S + E \xrightleftharpoons[k_s^-]{k_s^+} ES \xrightarrow{k_{cat}} E + P$$

$+ \qquad +$

$S \qquad S$

$k_{ss}^- \upharpoonleft\downharpoonright k_{ss}^+ \qquad k_{ss}^- \upharpoonleft\downharpoonright k_{ss}^+$

$$S + SE \xrightleftharpoons[k_s^-]{k_s^+} SES \xrightarrow{bk_{cat}} SE + P$$

Figure 1. Y. Cheng, J. Suen, Z. Radić, S. Bond, M. Holst and J. Andrew McCammon.

Fig. 2.

(a)



(b)

$$A + R^0 \begin{array}{c} \xrightarrow{k_{+1}} \\ \xleftarrow{k_{-1}} \end{array} AR^1 + A \begin{array}{c} \xleftarrow{k_{+3}} \\ \xrightarrow{k_{-3}} \end{array} C \begin{array}{c} \xrightarrow{\alpha} \\ \xleftarrow{\beta} \end{array} O$$

$$A + R^0 \begin{array}{c} \xrightarrow{k_{+2}} \\ \xleftarrow{k_{-2}} \end{array} AR^2 + A \begin{array}{c} \xrightarrow{k_{+4}} \\ \xleftarrow{k_{-4}} \end{array} C$$
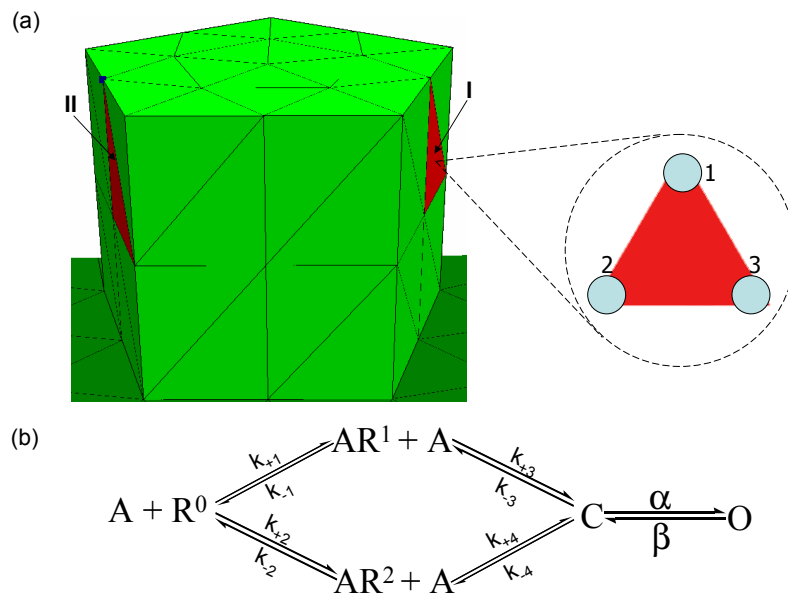
Figure 2. Y. Cheng, J. Suen, Z. Radić, S. Bond, M. Holst and J. Andrew McCammon.

Fig. 3.

(a)

(b)
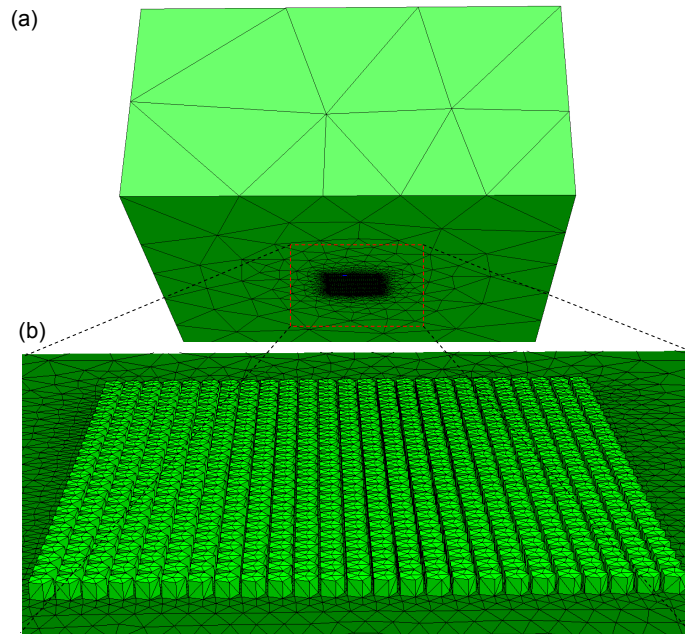


Figure 3. Y. Cheng, J. Suen, Z. Radić, S. Bond, M. Holst and J. Andrew McCammon.

Fig. 4.



(a)

0.10

0.10    0.30

0.25

0.40

0.35

(b)

(c)
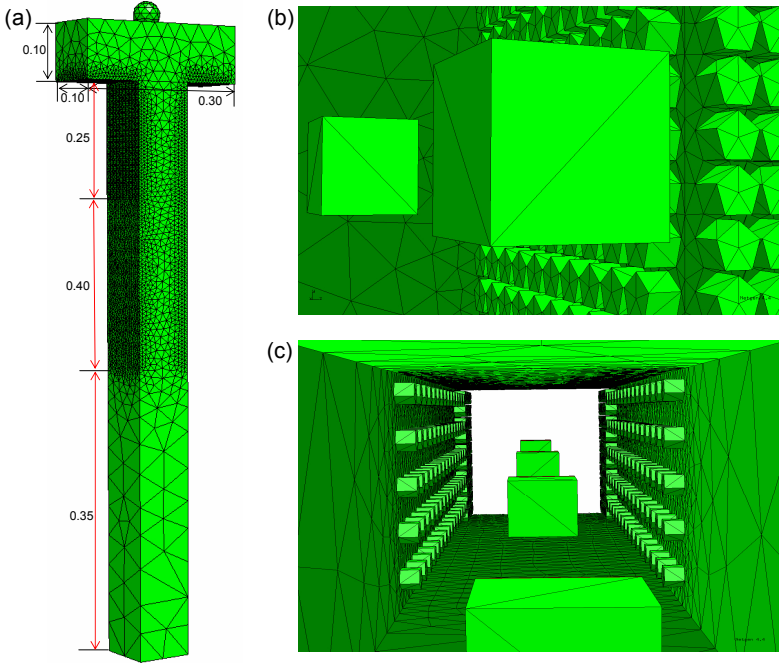
Figure 4. Y. Cheng, J. Suen, Z. Radić, S. Bond, M. Holst and J. Andrew McCammon.
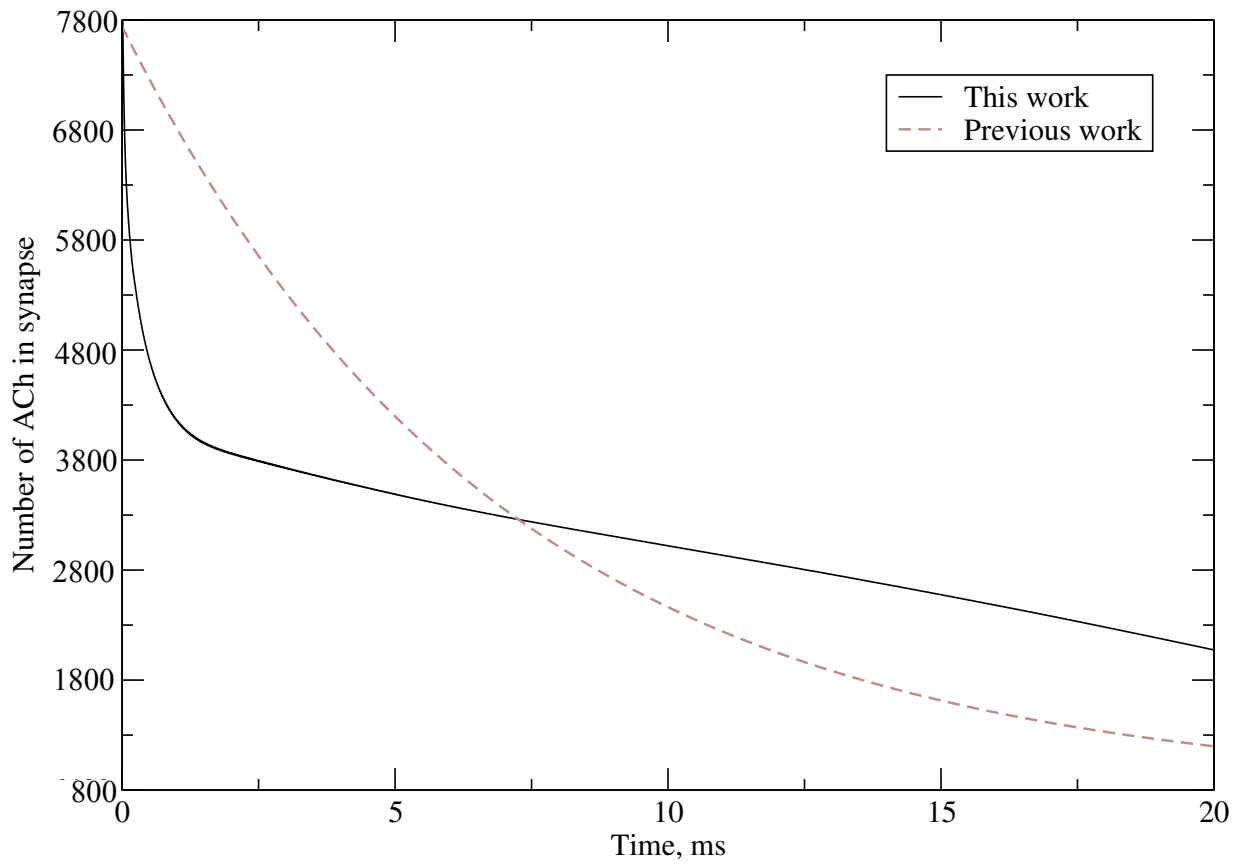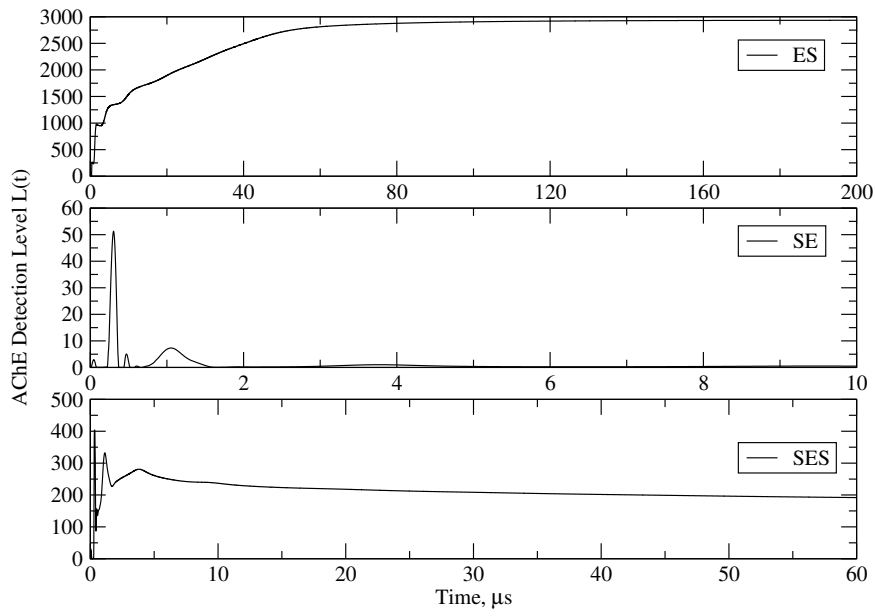
Fig. 5.

(a)

(b)

2.0

0.8

0.95

0.1
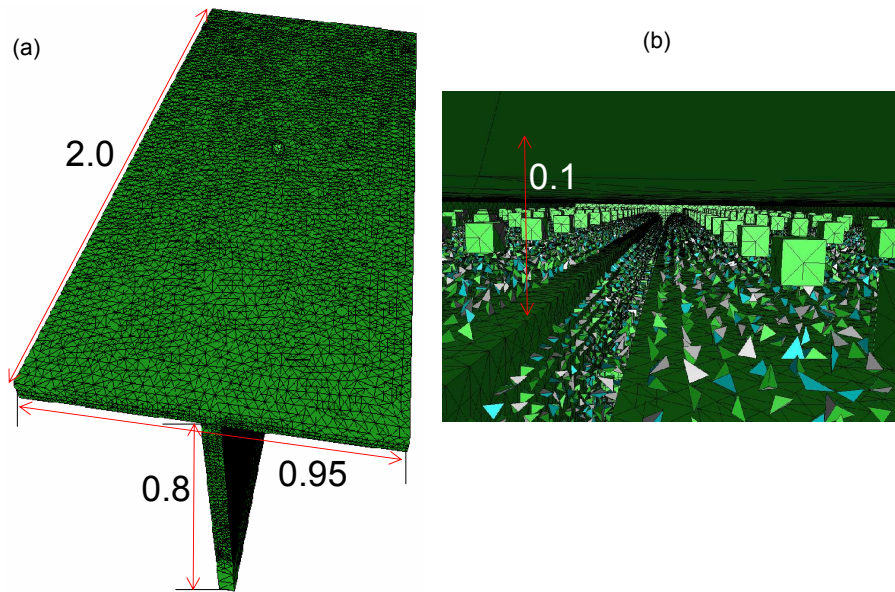
Figure 5. Y. Cheng, J. Suen, Z. Radić, S. Bond, M. Holst and J. Andrew McCammon.
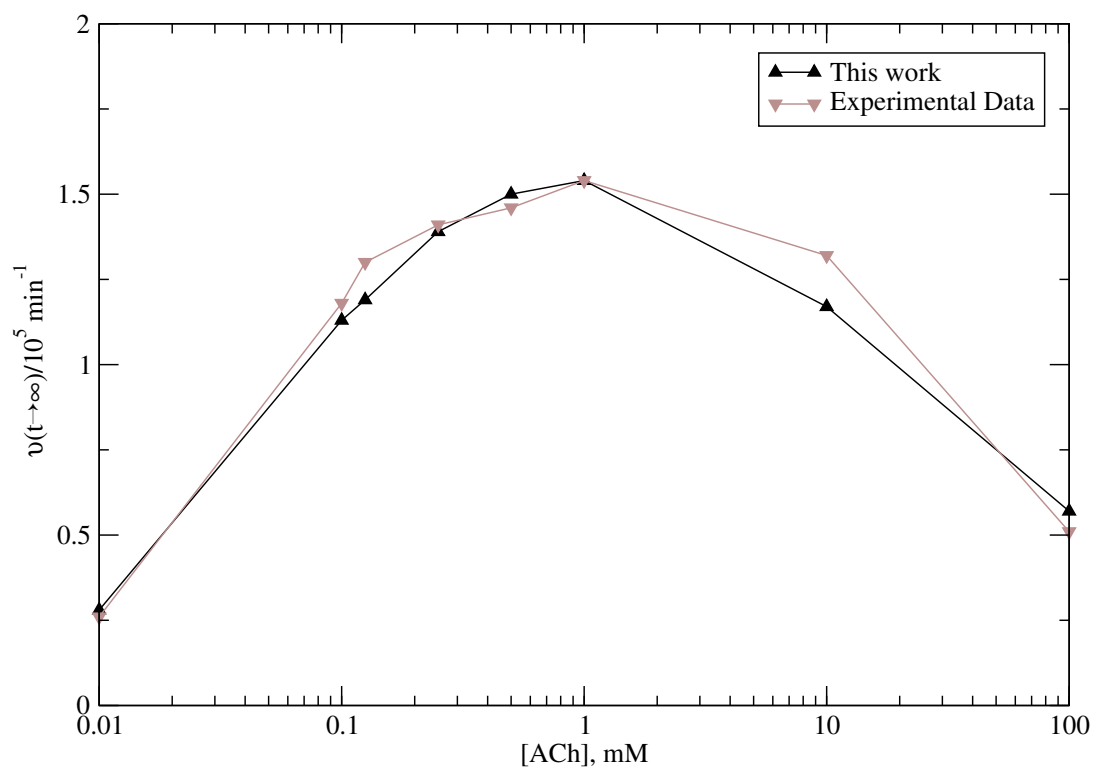
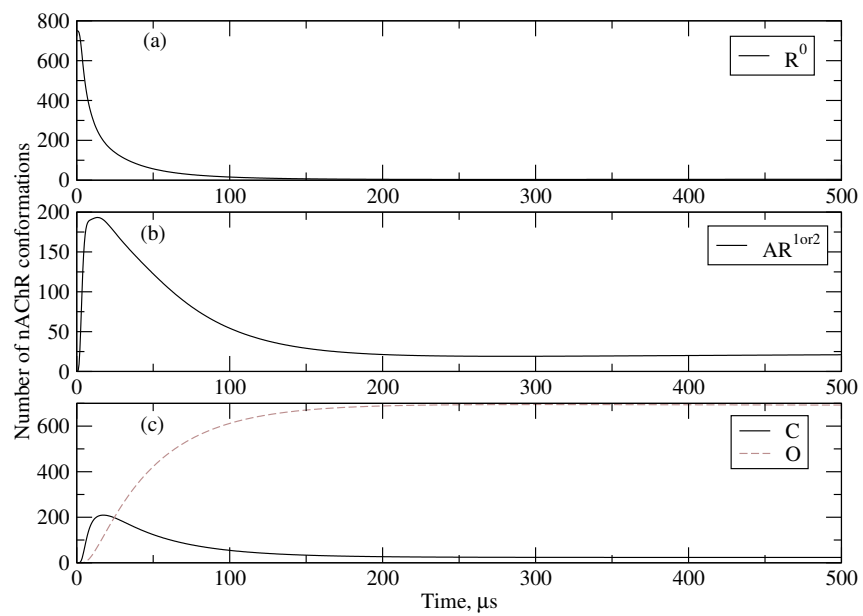Figure 6. Y. Cheng, J. Suen, Z. Radić, S. Bond, M. Holst and J. Andrew McCammon.
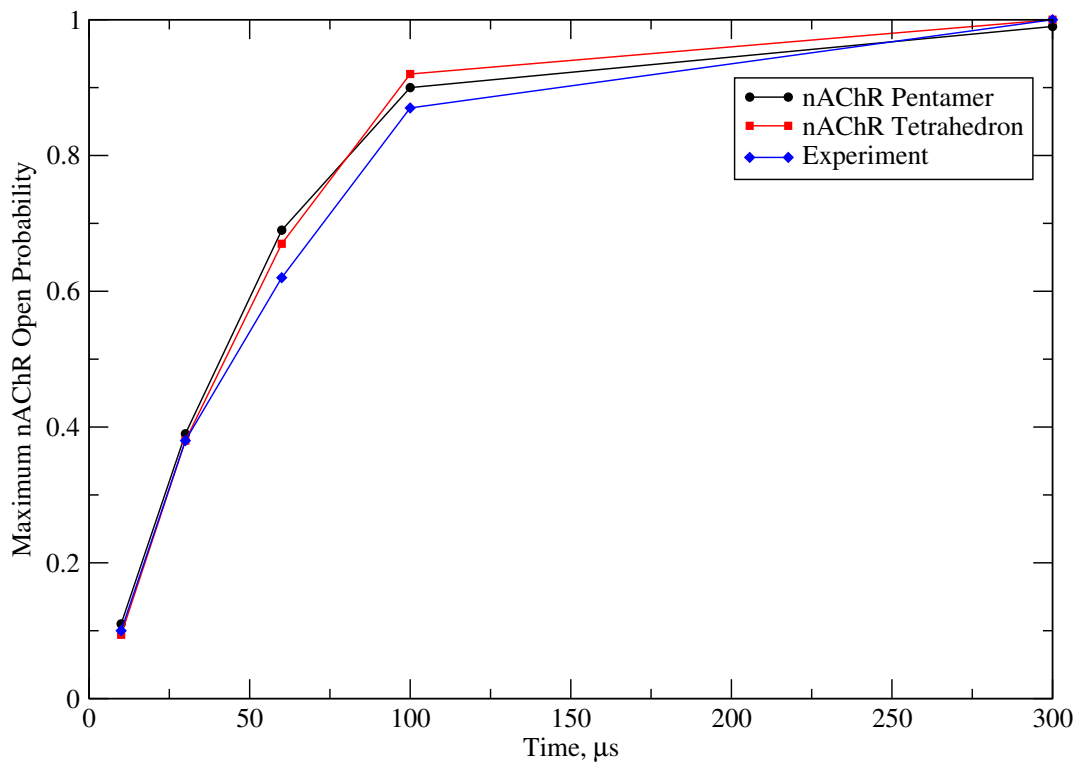
Figure 7. Y. Cheng, J. Suen, Z. Radić, S. Bond, M. Holst and J. Andrew McCammon.

Fig. 8.



Figure 8. Y. Cheng, J. Suen, Z. Radić, S. Bond, M. Holst and J. Andrew McCammon.

Figure 9. Y. Cheng, J. Suen, Z. Radić, S. Bond, M. Holst and J. Andrew McCammon.
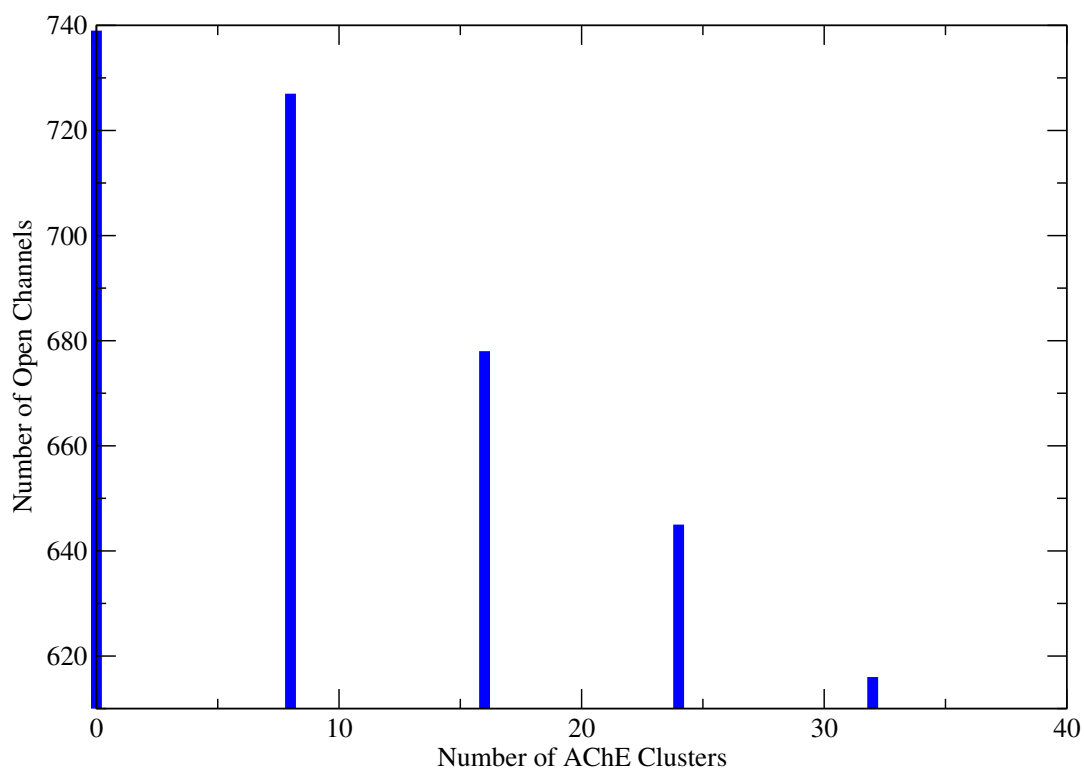
29

Figure 10. Y. Cheng, J. Suen, Z. Radić, S. Bond, M. Holst and J. Andrew McCammon.

30

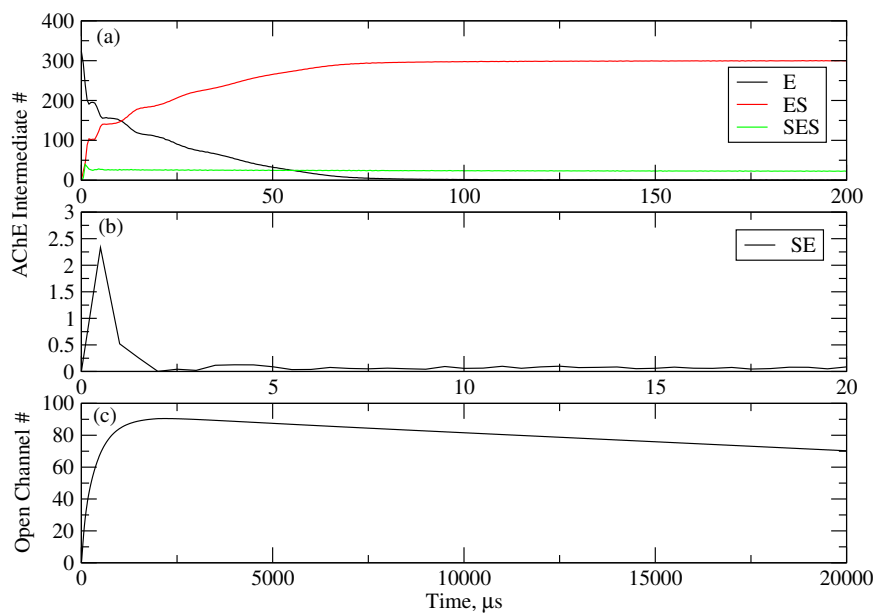Figure 11. Y. Cheng, J. Suen, Z. Radić, S. Bond, M. Holst and J. Andrew McCammon.

Figure 12. Y. Cheng, J. Suen, Z. Radić, S. Bond, M. Holst and J. Andrew McCammon.